Journal of Power Sources 195 (2010) 3224–3230

Contents lists available at ScienceDirect

Journal of Power Sources

journal homepage: www.elsevier.com/locate/jpowsour

A novel design for a flow field configuration, of a direct methanol fuel cell

Shou-Shing Hsieh*, Ho-Chieh Wu, Bing-Shyan Her

Department of Mechanical and Electro Mechanical Engineering, National Sun Yat-Sen University, Kaohsiung 80424, Taiwan, ROC

ARTICLE INFO

Article history:
Received 7 October 2009
Received in revised form
17 November 2009
Accepted 25 November 2009
Available online 1 December 2009

Keywords:
Flow field
Crossover
Direct methanol fuel cell
Carbon dioxide gas bubble

ABSTRACT

We proposed and tested a new and novel arrangement for a direct methanol fuel cell consisting of one inlet for a methanol solution and four outlets for oxidant gas (air), in both the anode and cathode flow fields. It utilizes different operating temperatures of 40 °C and 60 °C, and different methanol solution flow rates of 5 ml min^{-1}, 10 ml min^{-1}, and 20 ml min^{-1}. Test results indicate a significant reduction in produced CO_2 gas in the anode flow channels and product water in the cathode flow channels; consequently, cell performance can be greatly improved. Furthermore, methanol crossover can also be avoided and reduced.

1. Introduction

The term micro-fuel cell has been used to describe a fuel cell fabricated by the use of MEMS technology. A micro-fuel cell system benefits from this technology since the fuel cell acts as a miniature electrochemical reactor. The use of microtechnology for power generation has been the focus of many research groups [1–6]. Such research has already enabled the miniaturization of methanol fuel cells into compact micro-direct methanol fuel cells (μDMFCs) [4].

Micro-direct methanol fuel cells (μDMFCs) using polymer electrolyte membranes such as Nafion show promise as portable power sources for applications ranging from cell phones to laptop computers. There has been an increased interest in DMFCs within the last decade as these use liquid methanol solution fuels directly, with no reforming step necessary. Compared with other liquid fuel candidates, methanol shows better electrochemical activity and higher energy density. In addition, methanol solution fuels are much easier to store, transport and refill; μDMFCs usually have a compact design and up to 10 times the energy density of rechargeable batteries [4].

There are two main obstacles [5] hindering utilization of the DMFC. One is low performance resulting from poor kinetics of the electro-oxidation reaction of methanol in the anode. The other is the phenomenon of methanol crossover through the polymer electrolyte membrane from the anode to cathode side. Both diffusion and electro-osmotic drag of methanol contribute to methanol crossover. Due to the crossover, fuel utilization is reduced, degrades cathode performance and generates additional heat. Although attention has been given to these two problems, less has been given to issues such as the removal of anode gaseous products and cathode water [7–12].

The main functions of flow field plates are to act as a current collector and backing layer, to keep reactants separate, and to enable distribution of reactants. In addition, these plates allow removal of products (anode/cathode) over the reaction surface area [7,9]. Generally, there are pros and cons associated with the application of different flow field configurations. Proper selection of flow field geometry and size related to operating conditions can reduce costs and improve performance objectives. In addition, the liquid methanol solution in anode flow channels has to face a two-phase flow, namely, liquid fuel and transport of CO_2 gases. Similarly, the air/oxygen gas in cathode flow channels must also facilitate two-phase mass transfer, i.e., transport of both gaseous fuel and product water. Therefore, flow field design and configuration strongly influence the performance and stability of a DMFC.

In this work, a new and novel design was proposed consisting of one inlet of methanol solution and four outlets of air, applied to both the anode and cathode in a serpentine (meandering) flow channel configuration. A new flow field plate was fabricated and tested, and then examined for current-usage characteristics displayed within a wide range of operating temperatures and methanol solution flow rates. Simultaneously, a single transparent DMFC cell was assembled to allow observation of the evolution of product gaseous CO_2 in the anode and product water (H_2O) in the cathode.

* Corresponding author. Tel.: +886 7 5252000x4215; fax: +886 7 5254215.
E-mail address: sshsieh@faculty.nsysu.edu.tw (S.-S. Hsieh).

0378-7753/$ – see front matter © 2009 Elsevier B.V. All rights reserved.
doi:10.1016/j.jpowsour.2009.11.119

Table 1
Geometric parameters and operating conditions of the study.

Geometric parameters		
	One-outlet	Four-outlet
Number of inlet	1	1
Number of outlet	1	4
Channel width (mm)	1.0	1.0
Channel depth (mm)	0.25	0.25
Rib width (mm)	1.0	1.0
Hydraulic diameter (mm)	0.4	0.4
Cross-section area (mm^2)	0.25	0.25
Channel length (mm)	259	56 × 4
Open ratio (%)	51	45
Channel pass	10	4 × 4
Channel number	1	1 × 4
Active fuel cell area (cm^2)	5	5
Operating conditions		
	For performance test	For visualization test
Anode (methanol solution)		
Concentration (M)	1	1
Temperature (°C)	25[a]	
	40	40
	60	60
Flow rate (sccm)	5	5
	10	
	20	20
Cathode (air)		
Flow rate (sccm)	760	760
		610
		460
		300
		150
Electronic load		
Current density ($mA\,cm^{-2}$)		100
		200
		300
		400
		500

[a] Methanol solution flow rate is 0.1 sccm, 0.5 sccm, 1.0 sccm, 5 sccm and 10 sccm, respectively.

2. Experimental

2.1. New flow field plate and transparent fuel cell preparation

To study the influence of this new and novel design, a one inlet, four-outlet configuration for methanol fuel and air was fabricated. The design adhered to the relevant geometrical parameters for both anode and cathode flow channels as listed in Table 1. Furthermore, in order to observe CO_2 gas bubbles in the anode flow channels and product water in the cathode flow channels, a transparent DMFC was designed and fabricated as depicted in Fig. 1(a). A schematic diagram of the transparent DMFC with illustration of the methanol solution and oxidant gas (i.e., air) passage is presented. A copper (Cu) sheet 0.25 mm thick, sputtered with 2 nm gold ultra-thin film acting as a passivating layer to prevent corrosion, was used as the flow field plate and current collector. Acrylic (PMMA) glass was the transparent material used outside the flow field. Varied channel widths were designed and chosen/assembled in a serpentine fashion within a range of 800–2000 μm. The assembled prototype transparent DMFC (see Fig. 1(b)) consisted primarily of two end plates, two flow field channels/current collectors (see Fig. 1(a)), two gaskets and one membrane electrode assembly (MEA).

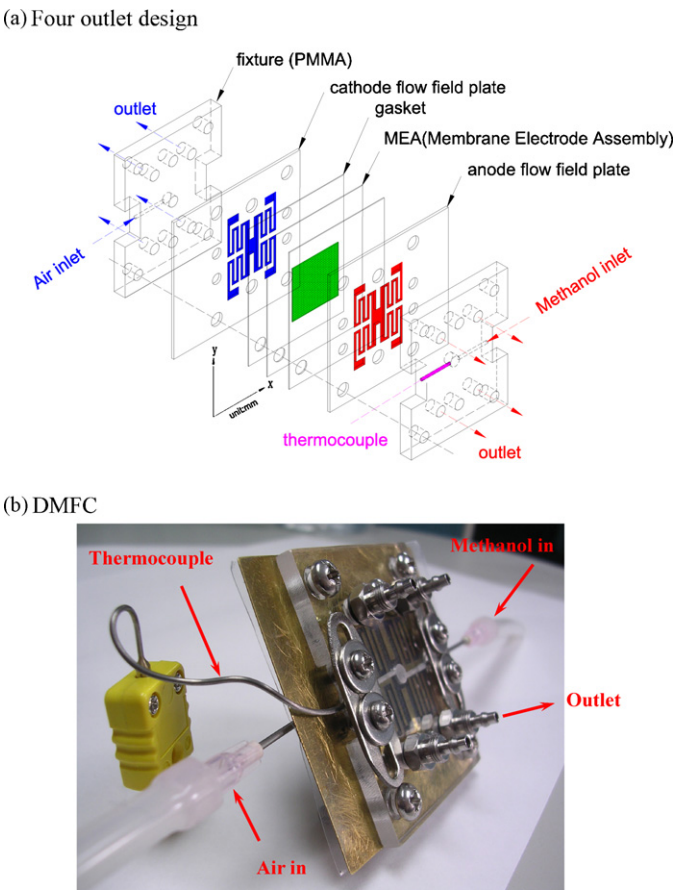

Fig. 1. Schematic illustration of new flow field design and associated images for DMFC: (a) Four-outlet design and (b) DMFC.

In this study, a common Nafion 115 membrane made by Dupont with an active area of 2.25 cm × 2.25 cm was employed. The catalyst loading on the anode side was 4.0 mg cm^{-2} with 40 wt.% Pt Ru alloy (1:1 a/o) on Vulcan XC-72, whereas the catalyst loading on the cathode side was 2.0 mg cm^{-2} with 40 wt.% Pt on Vulcan XC-72.

Transparent acrylate, used to fabricate the end plate, allowed observation of the formation of CO_2 bubbles at the anode and water flooding at the cathode.

2.2. Experimental system setup and operating conditions

The experimental system setup and flow loop for the study of a transparent DMFC and visualization of CO_2 bubbles in the anode and product water in the cathode are shown in Fig. 2. The setup consisted of an electronic load system (Arbin BT 2000), a peristaltic pump (Jason Servo Co Ltd, KT M4-001), and one mass flow controller (MKS M1008), two pre-heaters with temperature controllers, pressure relief valves, and pressure gauges. The electronic load system was used to characterize the polarization behavior of the fuel cell. A Sony digital video camcorder was used for flow visualization, with still pictures captured according to the time sequence during subsequent editing. In addition, with the fuel cell illuminated by a 100 W halogen spot lamp, a Nikon N70 camera captured images of CO_2 bubbles within a single anode channel at 60 fs^{-1}.

To avoid the accumulation of produced CO_2 gas in the anode flow channel and liquid water in the cathode flow channel, the methanol solution entered the anode flow field from the right lateral side, while air was fed into the cathode flow field from the left

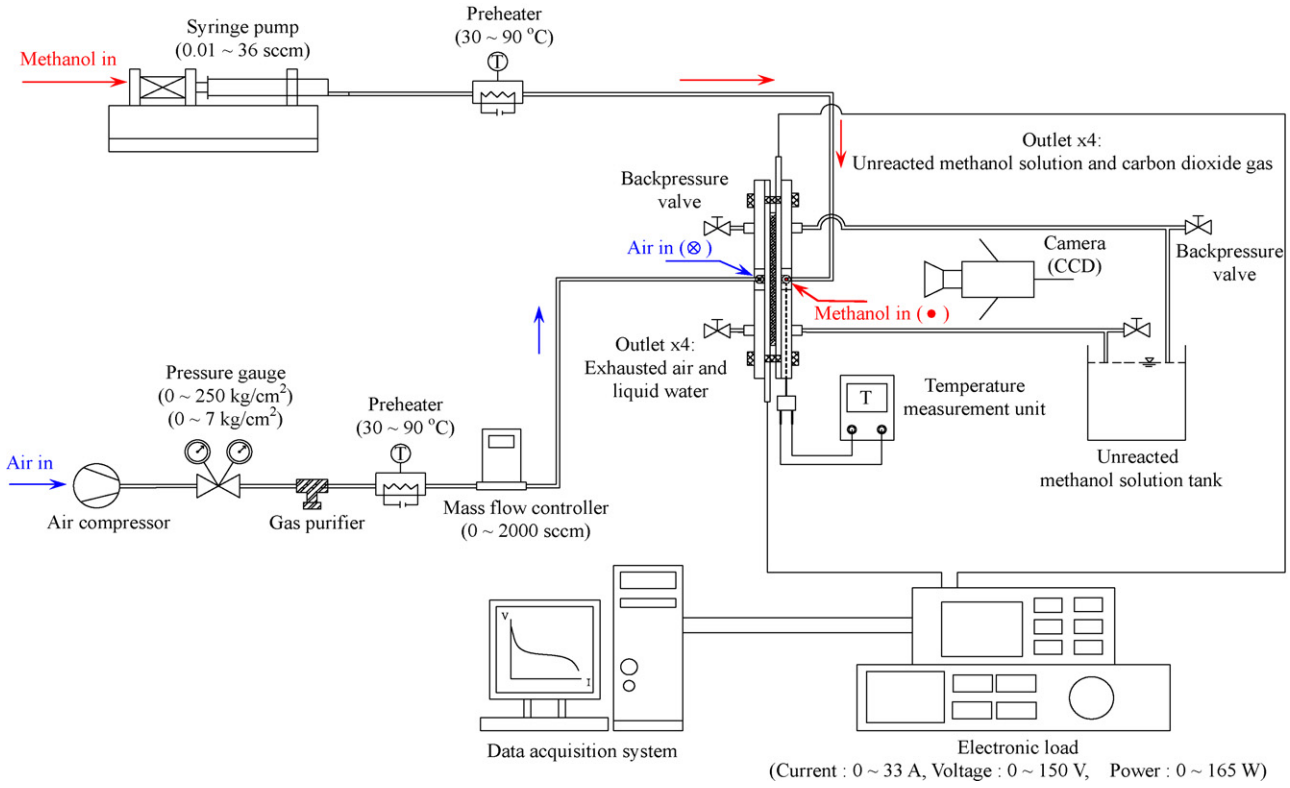

Fig. 2. Schematic of the flow loop.

lateral side (see Fig. 1(b)). All experiments were conducted under the same operating conditions, with the fuel cell positioned vertically. Other experimental conditions for performance tests and observation of CO_2 gas bubbles within the anode channels and visualization of product water in the cathode channels are listed in Table 1. Computer programs custom-written in Labview were used to control the experiments as well as to generate polarization and power density curves.

The performance of the DMFC under different operating parameters was measured. The cell was connected to an electronic load to draw current. A waiting period of about 50 s was used to obtain a steady state for each set of readings taken. The operating temperature of the DMFC was measured by a K-type thermocouple implemented with a data logger. Prior to experimental tests, the MEA was activated to improve the proton conductivities of both the MEA and the electrode following the directives of Meng and Kim [6]. All of the experiments were conducted under ambient conditions (25 °C, 97 kPa). The performance of the present DMFC with the new flow field design was recorded and the results compared to those of conventional fuel cells operating within the relevant operating parameters.

Table 2
Measurement variables uncertainty.

Items	Range	Error
DC volt	0–15 V	±0.06%
DC current	0–3.3 A	±0.06%
CO_2 gas bubbles accumulation	0–29.4%	±2.23%
Product water accumulation	0–50.7%	±2.46%

2.3. Measurements and associated uncertainty

Measurement data allow examination of the feasibility and practical applicability of this novel and innovative design via VI/PI performance tests, and through quantitative measurements of CO_2 gas bubble emergence in anode channels and product water (H_2O) accommodation in cathode channels. Each measurement was repeated at least five times with the deviation among them being ±5%. Averages were then determined and recorded. Table 2 lists the degree of uncertainty associated with relevant parameters and variables measured in this study.

Table 3
Comparison of the performance between four-outlet and one-outlet.

Operating conditions												
Methanol concentration(M)	1											
Cathode air flowrate(sccm)	760											
Temperature(°C)	40						60					
Anode methanol flowrate(sccm)	5		10		20		5		10		20	
Performance												
Number of outlet	1	4	1	4	1	4	1	4	1	4	1	4
Max. current density(mA cm^{-2})	1313	1513	1302	1441	1300	1402	1214	1463	1349	1674	1611	1806
Max. power density(mW cm^{-2})	196	266	180	228	175	210	179	211	210	244	254	271
Ratio of max. current density	1.15		1.11		1.08		1.21		1.24		1.12	
Ratio of max. power density	1.36		1.27		1.20		1.18		1.16		1.07	

3. Results and discussion

3.1. Performance tests

Polarization curves of the transparent fuel cell were extensively measured under different operating conditions as listed in Table 1. Fig. 3(a) and (b) shows cell performance using the new deign. The operating conditions included 1 M of aqueous methanol solution for the anode and air at 97 kPa for the cathode. Fuel and air were preheated to 40 °C, and 60 °C, respectively. A comparison of data in Fig. 3(a) and (b) demonstrates that an increase in temperature enhances performance of the DMFC. This is due to an improved electrochemical reaction occurring at both the anode and cathode at the higher temperature of 60 °C. It is found that at the methanol volume flow rate of 10 sccm with the cell temperature at 60 °C, maximum current density is 1700 mA cm^{-2}, with a power density of 240 mW cm^{-2} at a voltage of 0.22 V in Fig. 3(b).

Fig. 3(a) also depicts performance of the cell when the methanol feeding rate of 20 sccm occurs at the same preheated temperatures. When compared to performance at a fuel feeding rate of 10 sccm, the open circuit voltage (OCV) at the corresponding cell temperature and a feeding rate of 20 sccm in Fig. 3(a) decreases somewhat. This is due to the methanol crossover from anode to cathode at the higher feeding rate.

During the experiments, the dynamic behavior of CO_2 gas bubbles including emergence, growth, coalescence, and formation of CO_2 gas slugs was similar at different cell temperatures. The quantity of CO_2 gas bubbles and large gas slugs increased in the channels at a higher cell temperature of 60 °C as compared to a cell temperature of 40 °C. Both Fig. 3(a) and (b) demonstrates that an increase in cell performance results in enhanced catalyst activity. The increased diffusion coefficient of liquid methanol counterbalances the buildup of CO_2 gas bubbles, resulting in an improvement in cell performance.

Similarly, it was found that as the liquid methanol solution flow rate was increased (e.g., 20 sccm) as shown in Fig. 3(a) and (b), individual CO_2 gas bubbles emerging into the channels became smaller, and the coalescent gas slugs became shorter (not shown). This also resulted in less gas bubble coverage. A more rapid electrochemical reaction than that which occurred when the flow rate was 10 sccm resulted from the easier and faster removal of CO_2 gas bubbles.

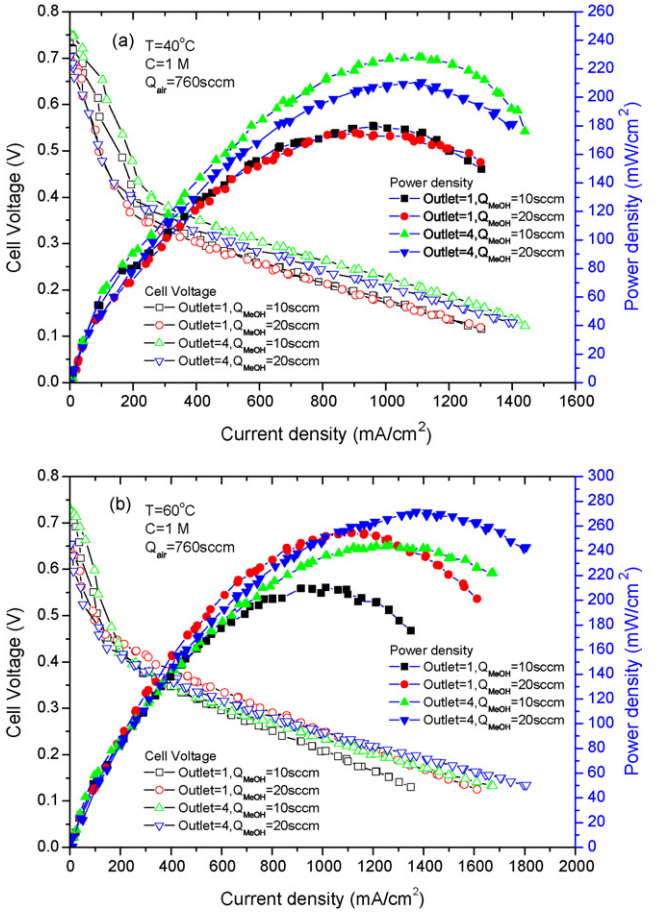

Fig. 3. Effect of operating temperature on performance of DMFC with 1 M methanol at (a) 40 °C and (b) 60 °C.

Also included in both Fig. 3(a) and (b) are the performance results using a traditional fuel cell design (single-outlet). It can be seen from both figures that cell performance with the traditional design is consistently lower than that of the new four-outlet

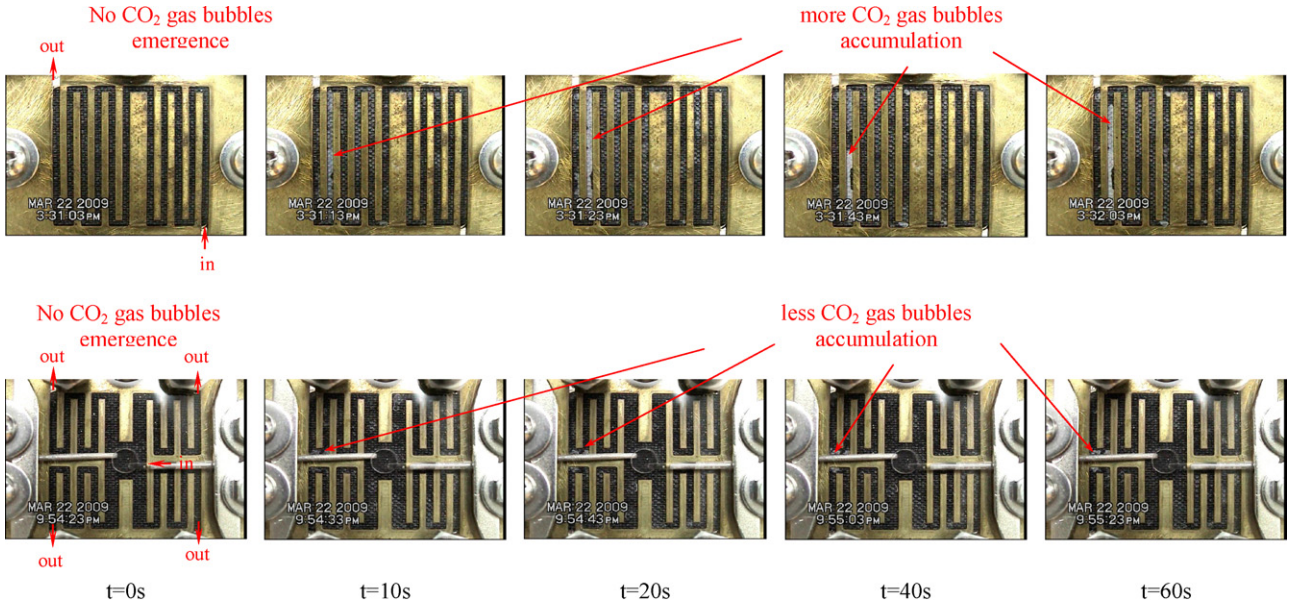

Fig. 4. Time evolution images of CO_2 gas bubbles (anode) for 1 M methanol solution with feed rate of 5 sccm at 40 °C (in/out stand for fuel in/out).

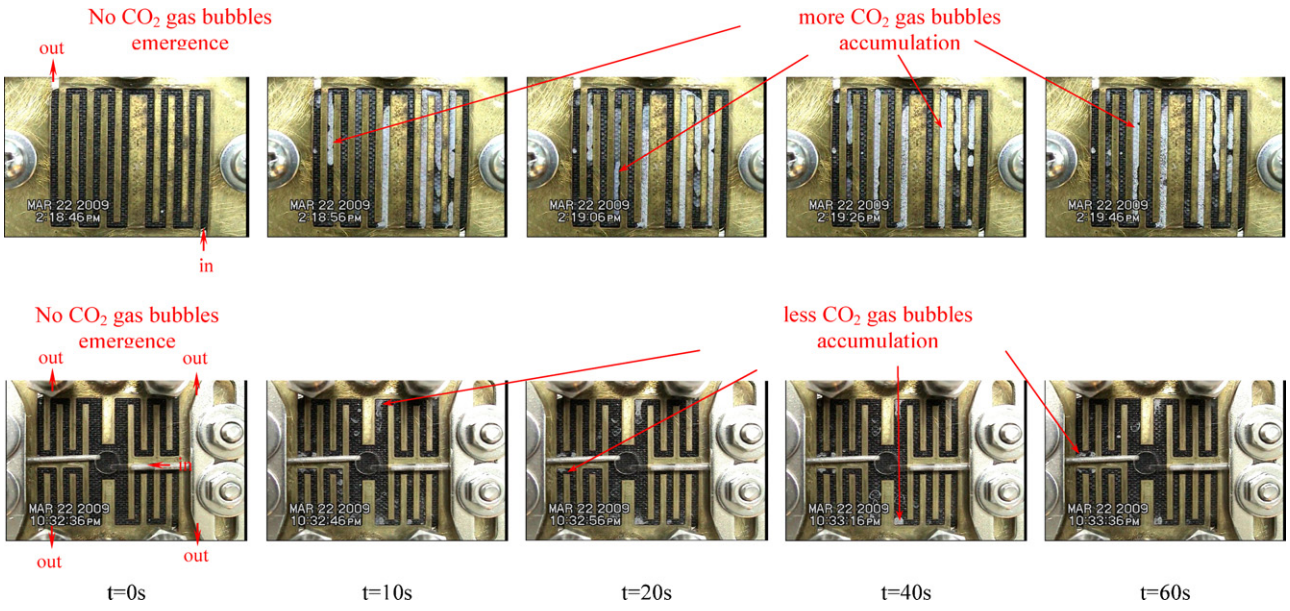

Fig. 5. Time evolution images of CO_2 gas bubbles (anode) for 1 M methanol solution with feed rate of 5 sccm at 60 °C (in/out stand for fuel in/out).

design. Table 3 lists quantitative comparisons for related parameters (e.g., maximum current and power density) of VI/PI curves under different operating conditions.

3.2. Visualization/quantification of CO_2 bubble dynamics on the anode

Figs. 4 and 5 display an image of CO_2 gas bubbles under conditions corresponding with those shown in Fig. 3(a) and (b) at a current density of 500 mA cm^{-2}. A set of time evolution images ($t \leq 60$ s) of CO_2 gas bubbles shows the dynamic behavior of the bubbles in a serpentine anode channel of the cell. Both single-outlet and four-outlet designs are shown. It can be seen that under the same operating conditions, there appear to be no CO_2 gas bubbles in the four-outlet flow channels at cell temperatures of either 40 °C or 60 °C. However, the conventional single-outlet flow channels do have CO_2 gas bubbles emerging around the corner as expected, due to active nucleation sites for CO_2 gas bubble emergence between the channel rib and the surface of the porous diffusion layer (DL) at the very beginning ($t \simeq 10$–20 s) of the downstream channels. Over time, CO_2 gas bubbles continually emerged at different locations on the porous DL surfaces and simultaneously previously formed bubbles grew larger. Following the growth of the CO_2 gas bubbles, they began to coalesce into even larger bubbles and expanded from the corner of the rib toward the center of the channel. This resulted in an increased area of bubbles to the point where they eventually occupied the entire channel gap with bubbles elongated along the channels. At 40 °C, this situation occurred in downstream channels, whereas at 60 °C, even upstream channels experienced bubble accumulation as indicated in Fig. 5.

At the same time, the flow patterns in Figs. 4 and 5 show that CO_2 gas slugs formed in the flow channels as a result of merging upstream bubbles. Between the passing of CO_2 gas bubbled slugs, bubbles were observed to nucleate and grow rapidly at DL surfaces. As the bubble slugs were pushed by the liquid methanol solution and as they travelled downstream, these new bubbles nucleating on the DL walls were submerged into the bubble slugs, contributing to an elongation of the slugs. This is clearly evidenced in Fig. 5.

As outlined by Hussaini and Wang [9], quantification of the area of the anode channel covered by CO_2 gas bubbles can be calculated and obtained. These were plotted against current density as shown in Fig. 6 where a plot shows the CO_2 gas bubble area ratio at cell temperatures of 40 °C and 60 °C and different current densities in one-outlet and four-outlet flow channels. It is seen that at every combination of cell temperature and liquid methanol solution flow rate, there is a certain threshold current density ($\simeq$100 mA cm^{-2}) below which there are no CO_2 gas bubbles present in the liquid channels. Above this threshold, CO_2 gas bubbles emerge and tend to increase proportionately at different rates under different conditions. Basically, CO_2 gas bubble emergence and accumulation in four-outlet flow channels are much less than those in one-outlet flow channels. In Fig. 6, it can also be seen that at a given current density, an increase in the liquid methanol solution feed rate results in a decrease in the presence of CO_2 gas bubbles. This is because the CO_2 gas bubble production rate is much less than flow in carrying away rate at higher liquid methanol solution feed rate. Furthermore, an increase in cell temperature leads to an increase in the CO_2 gas bubble production rate so a four-outlet flow would be preferable.

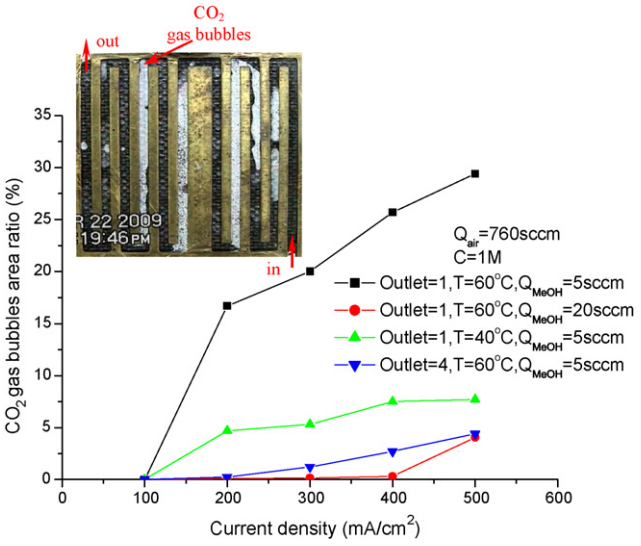

Fig. 6. CO_2 gas bubbles area ratio as a function of current density at different temperatures and for different number of outlet at different anode flow rate with 1 M methanol concentration.

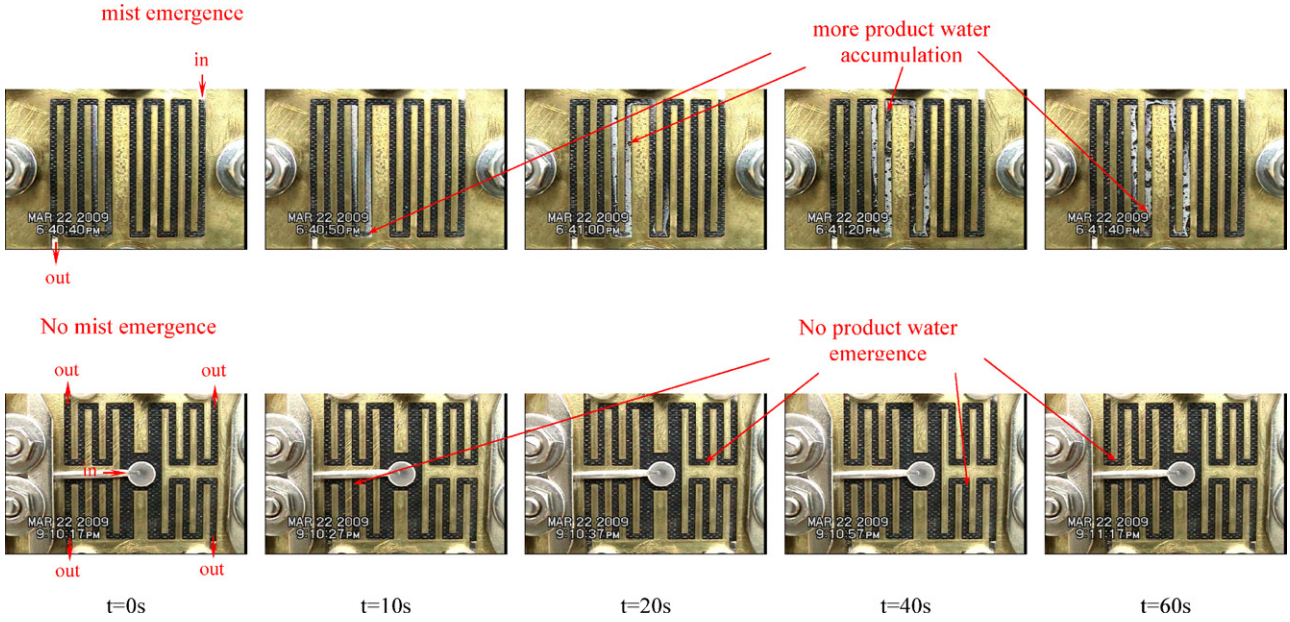

Fig. 7. Time evolution images of product water (cathode) for air of 760 sccm at 40 °C (in/out stand for air in/out) mist emergence

3.3. *Visualization/quantification of water flooding on cathode*

Generally, once the electrochemical reaction takes place, water is produced in the cathode electrodes and transported to the flow channels. Figs. 7 and 8 show a sequence of frames obtained by the study for water accumulation in single and four-outlet flow channels at a cell temperature of 40 °C and 60 °C, respectively. The images were taken at 10 s intervals with the flow direction either upward/or downward. The channels initially appeared foggy, as shown in Fig. 7, at a cell temperature of 40 °C in single-outlet flow channels at $t \leq 10$ s. Over time, these fog droplets accumulated and coalesced on the channel floor (i.e., DL surface) as small droplets about 0.4 mm in diameter. The water droplets expanded and eventually occupied the entire cross-section of the channel, with intermittent liquid slugs occurring between successive expanding droplets. Thus, as observation time progressed, two-phase flow patterns evolved. More detailed flow morphology can be explained as follows.

The water and air mixture two-phase flow regime was initially characterized by isolated droplets occurring within the flow ($t \leq 20$ s). As these droplets coalesced, bullet-shaped slugs of vapor (slug flow) were formed as $t \leq 30$ s; these occupied nearly the entire cross-section of the flow channel. Further up, or down the channel, these slugs grew together to form a continuous vapor core within the center of the flow channel, with a climbing liquid film covering the channel wall. This is called annular flow ($t \leq 40$ s). Higher up the channel, the shear stress on the free surface of the slow-flowing water film caused waves to form, resulting in possible entrainment of water droplets in the air core. All of the results for the single-outlet channels at a cell temperature of 40 °C can be seen in Fig. 7.

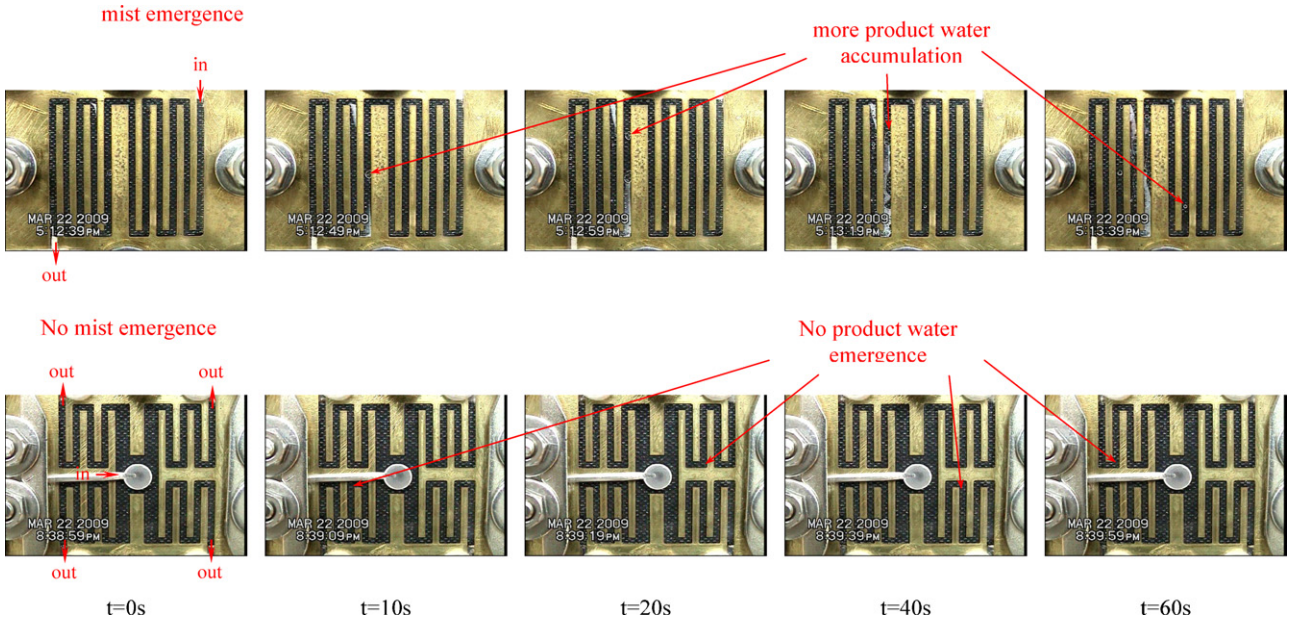

Fig. 8. Time evolution images of product water (cathode) for air of 760 sccm at 60 °C (in/out stand for air in/out).

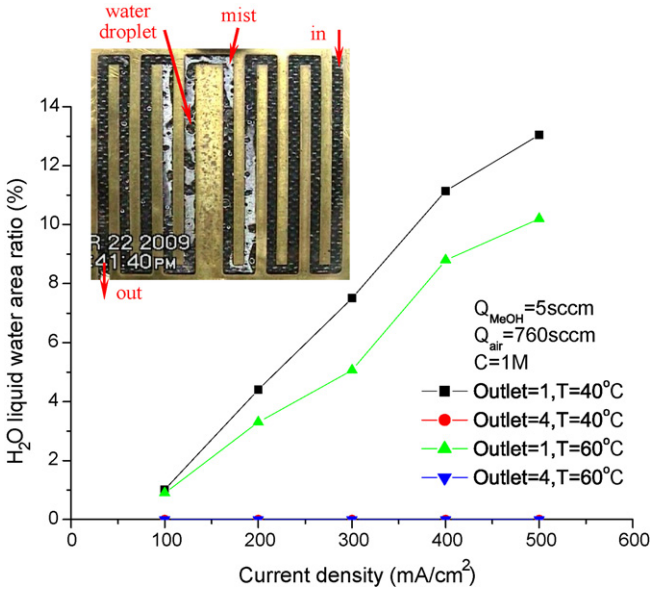

Fig. 9. H_2O liquid water area ratio as a function of current density for different number of outlets and temperatures with 1 M methanol concentration at 5 sccm and air flow rate at 760 sccm.

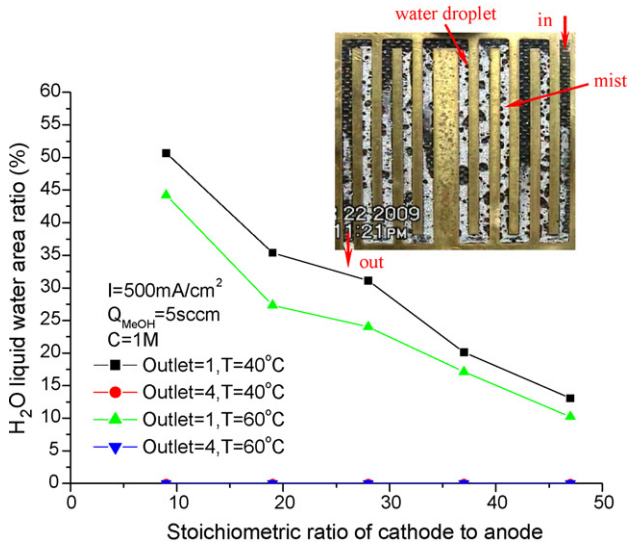

Fig. 10. H_2O liquid water area ratio as a function of stoichiometric ratio of cathode to anode with 1 M methanol concentration at 5 sccm for different number of outlets and temperatures.

However, as strongly evidenced in Fig. 7, the above stated situation did not seem to occur in the four-outlet flow channels. As shown in Fig. 8, product water accumulation in the single-outlet flow channels became severe as the cell temperature increased to 60 °C. Again, the flow morphology evolution looks similar to that shown in Fig. 7. The present four-outlet flow channel design did not display the emergence of any product water as one would expect when comparing data to that in Fig. 7.

Again, following the definition of a wetted area fraction rate [9], Fig. 9 shows a plot of an H_2O liquid ratio as a function of current density at two different cell temperatures for two outlet configurations at $t \leqq 60$ s. It is interesting to note that there was almost no product water accumulation in four-outlet flow channels regardless of the cell temperature at this low liquid methanol solution feed rate of 5 sccm. On the contrary, one-outlet flow channels did have product water accumulation which seemed to increase proportionately with a current density increase. Again, a definite threshold value of current density was found to be 100 mA cm^{-2}. Although the production rate may be higher at a higher cell temperature, a lower H_2O (liquid water) area ratio (possibly due to rapid evaporation) as a function of the stoichiometric ratio defined in [9] was read from Fig. 10 as compared to the proportion of wetted area at a lower cell temperature and a specific current density. Finally, the H_2O (liquid water) area ratio was plotted against the flow stoichiometry ratio at two different cell temperatures for one and four-outlet flow channel configurations, as shown in Fig. 10. Again (as shown in Fig. 9), four-outlet flow channels did not show any water accumulation even at a much higher current density of 500 mA cm^{-2}. However, one-outlet flow channels exhibited a definite behavior of a nearly linear decrease in the wetted area ratio as the stoichiometry ratio increased. Also included in Figs. 6, 9 and 10 are insets of images depicting CO_2 gas bubble (see Fig. 6) and product water (see Figs. 9 and 10) emergence in flow channels where the maximum values of gas bubbles and product water were marked for reference.

4. Conclusion

A novel and innovative four-outlet flow channel configuration was designed, fabricated, and tested within a range of related parameters. It was found that the present four-outlet flow channel design has remarkable capability for removing CO_2 gas bubbles and product water in anode/cathode flow channels, respectively. Consequently, significant improvement in corresponding cell performance has been secured. Additionally, this new design may change the conventional fuel cell flow field design philosophy, which would impact the fuel cell fabrication processes.

References

[1] S.S. Hsieh, J.K. Kuo, C.F. Huang, H.H. Tsai, Microsyst. Technol. 10 (2004) 121–126.
[2] A. Kamitani, S. Morishita, H. Kotaki, S. Arscott, J. Power Sources 187 (2009) 148–155.
[3] W. Qian, D.P. Wilkinson, J. Saeu, H. Wang, J. Zhang, J. Power Sources 654 (2006) 202–213.
[4] S. Hikita, K. Yamane, Y. Nakajima, JSAE Rev. 22 (2001) 151–156.
[5] S.H. Chan, N.T. Nguyen, Z. Xia, Z. Wu, J. Micromech. Microeng. 15 (2005) 231–236.
[6] D.D. Meng, C.J. Kim, J. Power Sources 194 (2009) 445–450.
[7] G.Q. Lu, C.Y. Wang, J. Power Sources 134 (2004) 33–40.
[8] K.G. Stanley, E.K. Czyzewska, P.K. Vanderhoek, L.Y. Fan, K.A. Abel, Q.M. Wu, M. Parameswaron, J. Micromech. Microeng. 15 (2005) 1979–1987.
[9] I.S. Hussaini, C.Y. Wang, J. Power Sources 187 (2009) 444–451.
[10] Q. Liao, X. Zhu, X. Zheng, Y. Ding, J. Power Sources 171 (2007) 644–651.
[11] J. Han, H. Liu, J. Power Sources 164 (2007) 166–173.
[12] H. Yang, T.S. Zhao, Q. Ye, J. Power Sources 139 (2005) 79–90.